Chapter 2

Fast Nonlinear Ion Transport via Field-Induced Hydrodynamic Slip in Sub-20 nm Hydrophilic Nanofluidic Transistors

2.1 Introduction

Recently, novel fluid-mechanical phenomena have been observed as the dimensions of fluidic channels have approached the nanometer scale. Theoretical models[1-4] and experimental demonstrations[5-7] of finite hydrodynamic slip in hydrophobic nanochannels have received considerable attention; however, experimental evidence of slip in hydrophilic nanochannels is nonexistent. Here we report on ion transport through an array of 20 nm-radius, 20 μm-long hydrophilic SiO_2 nanofluidic transistors. Above a threshold source-drain bias, channel conductances are enhanced up to 50-fold over expected values. The improved ion transport is interpreted as arising due to an electric field-induced breakdown of the zero-slip boundary condition. The slip length can be tuned by modulating the surface-charge density of the nanochannels via application of a gate voltage. This phenomenon results in amino acid specific I-V traces when lysine and aspartate monomer solutions are added separately, which demonstrates the potential for

the use of nanofluidic channel devices for high throughput protein sequencing and structure determination. The presence of finite slip results in a ~10^6-fold increase in mechanical power output, and thus also shows promise for efficient energy conversion, filtration, and desalination applications.

The relatively recent emergence of nanochannel fabrication methods[8-10] has allowed electrokinetic phenomena to be investigated in nanofluidic systems, and has created renewed interest in the potential of fluidic devices for energy conversion and other tasks. As the Debye screening length approaches the scale of the channel dimensions, the surface charge dominates the electrokinetic flow behavior within the channel, controlling the concentration of electrolytes[11-16] such that unipolar counterions dominate current flow (**Figure 2.1**). This phenomenon can potentially be harnessed for mechanical-to-electrical energy conversion by using pressure to drive a streaming current through the nanochannel. Alternatively, electrical-to-mechanical energy conversion is possible by applying an electric field across the length of the nanochannel, thereby driving fluid through by electroosmosis[17-19]. However, current flow through nanofluidic channels at a given pressure, or source-drain voltage, is severely limited due to the no-slip boundary condition that characterizes most such systems. This boundary condition represents the fact that there is no fluid or ion flow at the liquid/channel interface. The counterion density is highest at this interface, but because these counterions are immobilized by surface charges, those ions do not contribute to the current, resulting in low energy conversion efficiencies.

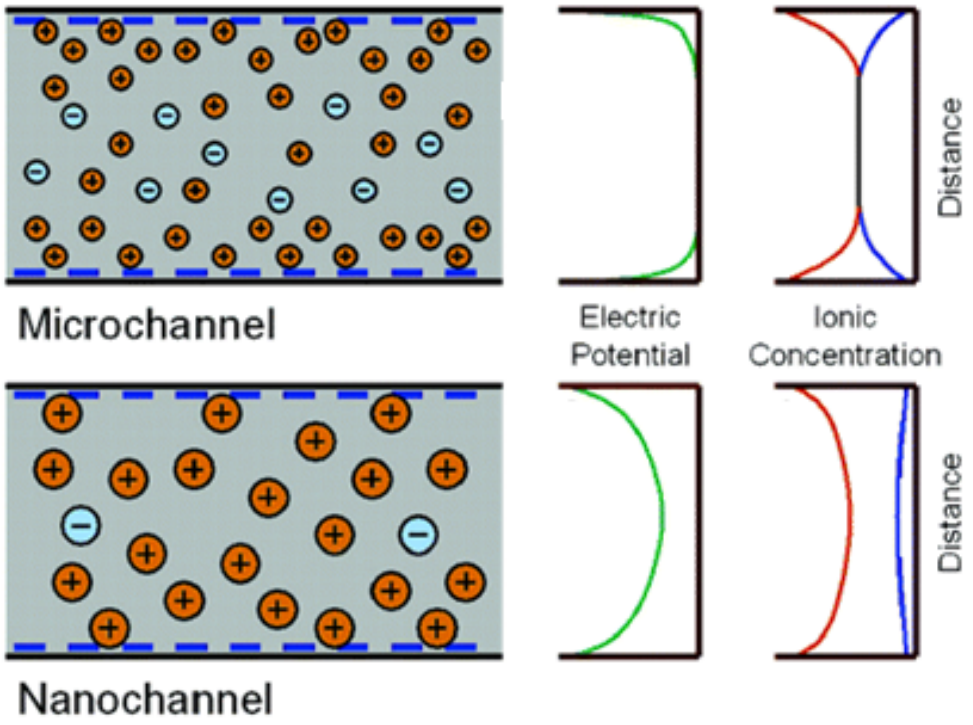

Figure 2.1. Nanochannel electrokinetics. At the nanoscale, channel dimensions become comparable to the Debye screening length, such that unipolar counterions in solution form an electric double layer and dominate current flow when channel surfaces are charged. This phenomenon only occurs below a threshold ion concentration. Adapted from *Nano Lett.* **2005**, 5, 943-948.

The no-slip boundary condition is not a fundamental limitation, however, and systems with finite slip have received recent attention[20,21]. Slip velocity (υ_{slip}) is proportional to the shear rate, according to the following equation:

$$\upsilon_{slip} = \mathbf{b}(d\upsilon/d\mathbf{x})|_{surf}.$$

Here, υ is the fluid velocity, **x** is the coordinate normal to the surface, and **b** is the slip length, or the distance into the surface where υ extrapolates to zero.

A number of theoretical studies[21,22] have revealed that mechanical-to-electrical energy conversion efficiencies can be very high, even approaching 100 %, for nanofluidic

channels exhibiting a large **b**. These studies have focused on streaming currents through smooth, hydrophobic nanofluidic channels, since such systems are thought to exhibit the greatest potential for slip. For example, Ren and Stein[21] have calculated that, for a 10 nm high slit-shaped, hydrophobic nanochannel, 40 % energy conversion efficiencies are realistic for **b** values of 30 nm. Indeed, very large slip lengths have been measured in carbon nanotube-based nanofluidic channels[5,7]. However such devices may not be suitable for energy conversion since the lack of surface charges prevents the creation of an intrachannel unipolar environment essential for mechanical-to-electrical energy conversion. Currently, most nanofluidic channels are fabricated from silica or other materials that yield charged and/or hydrophilic surfaces. Due to the strong attraction of Stern layer counterions to such hydrophilic surfaces, the no-slip condition is difficult to overcome. For example, Dekker's group has measured energy conversion in hydrophilic nanochannels under no-slip conditions, and found a conversion efficiency of only 3 %[23]. They calculated a maximum conversion efficiency of 12 % for similar monovalent ions in water[22]. Much greater conversion efficiencies will be needed for practical technologies to be realized. If the no-slip boundary condition in hydrophilic channels could be surmounted, greatly enhanced streaming currents and energy conversion efficiencies would be possible in such systems, making energy conversion applications far more feasible.

2.2 Experimental Methods

In this chapter, we report on the electrokinetics of potassium chloride (KCl) ion transport through nanofluidic transistors comprised of arrays of oval shaped, hydrophilic, silica nanochannels. Although ion transport has been investigated previously in a single SiO_2 nanofluidic channel[10] with similarly small dimensions, our fabrication method[24] produces sufficiently large numbers of closely spaced SiO_2 nanochannels such that currents can be measured even at very low KCl molarities ([KCl] = 10^{-7} M).

The experimental setup is shown in **Figure 2.2**. The nanofluidic device consisted of a 20 micrometer-long array of 80 parallel, 20 nm × 30 nm cross section silica channels built from a template of silicon nanowires fabricated using the SNAP method[24] (**Figure 2.2b,c**). An indium tin oxide (ITO) gate electrode is deposited on top of the array, with a silica gate oxide layer sandwiched in between. As shown in **Figure 2.2c**, extremely narrow (~3 nm) channels between the primary channels were observed. These likely arise from a SiO_2 deposition process that is not 100 % conformal. However, the voids are far smaller than the primary nanochannels and their contribution to the ionic current should be negligible. The nanochannels interface with two sets of microfluidic channels that act as reservoirs for electrolyte solutions. The device is sealed with a slab of plasma-bonded PDMS to isolate the microfluidic channels and prevent leakage current. Finally, holes are punched into the PDMS to allow the insertion of Ag/AgCl electrodes into the microfluidic channels for current measurements. The detailed fabrication processes are described in the Appendix. The SNAP-based nanochannel fabrication method is robust, allowing devices to be consistently generated with nearly 100 % yield.

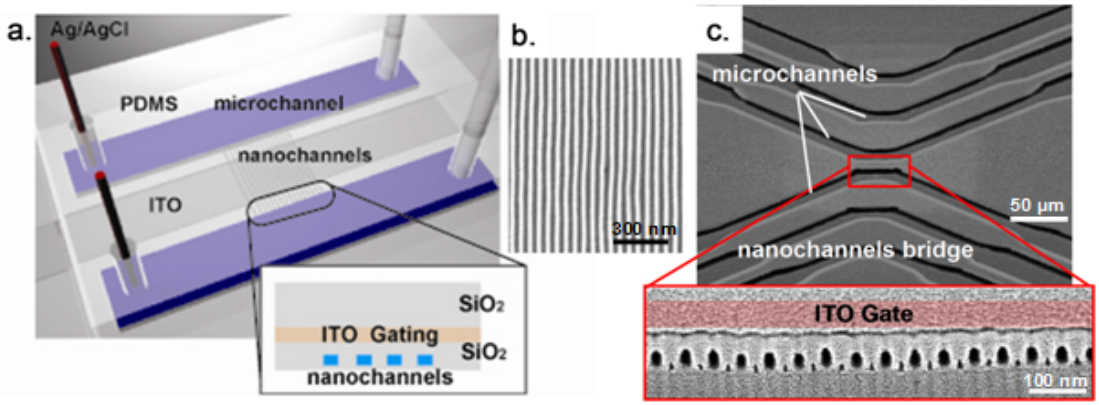

Figure 2.2. Overview of nanofluidic device. a. Experimental setup of essential components of the nanofluidic transistor array. The blue microchannels are electrically contacted with Ag/AgCl source and drain electrodes. These microchannels are connected via a bridge of 80 nanofluidic channels in SiO_2. As shown in the inset, the nanochannels are topped with an indium tin oxide (ITO) gate electrode. **b.** Scanning electron micrograph (SEM) of the silicon nanowire array (top view) from which the SiO_2 nanochannels were templated. **c.** SEM of the nanofluidic device. The 6 V-shaped structures are microfluidic channels; only the two opposing microchannels in the central region of the image are utilized for these experiments. These two channels are bridged by the 20 μm long nanofluidic channel array. Below, an end-on SEM view of a few of the (20 nm wide × 30 nm high) nanofluidic channels is shown, with the position of the ITO gate electrode indicated.

2.3 Results and Discussion

2.3.1 Slip-enhanced ion transport through nanofluidic channels

Upon completion of device fabrication, we introduced aqueous solutions of KCl into the device at concentrations ranging from 10^{-7} M to 10^{-1} M, optically observed nanochannel filling over the entire array, and measured the source-drain current-voltage (I_{SD}-V_{SD}) characteristics over a 30 – 50 volt range (conductance plots (dI_{SD}/dV_{SD}) at the abovementioned KCl concentrations are presented in the Appendix). Similar to previous studies[12,13], which were limited to conductance measurements at low bias (< 5 V),

conductance saturation is present below a threshold concentration of 10^{-3} M. This saturation occurs because the negatively charged silanol groups at the SiO_2 nanochannel surface attract K^+ counterions and repel Cl^- anions over the characteristic Debye length (κ^{-1}), which is given by[25]:

$$\kappa^{-1} = [\varepsilon k_B T/(e^2 N_A \Sigma_i c_i Z_i^2)]^{1/2}.$$

Here, c_i is the molar concentration and Z_i is the valence of ion species *i*. Standard constants include ε (the permittivity), k_B (Boltzmann constant), e (electron charge), and N_A (Avogadro's number). For [KCl] = 10^{-3} M, this gives a Debye length of 9.7 nm, which is comparable to the 10 nm radius of our nanochannels. As a result, the K^+ concentration within our nanochannels is determined by the surface charge on the walls for bulk [KCl] $\leq 10^{-3}$ M. On the other hand, for [KCl] > 10^{-3} M, the Debye length becomes smaller than the nanochannel radius, leading to shielding of surface charges and more ohmic ion transport behavior (**Figure 2.3b**).

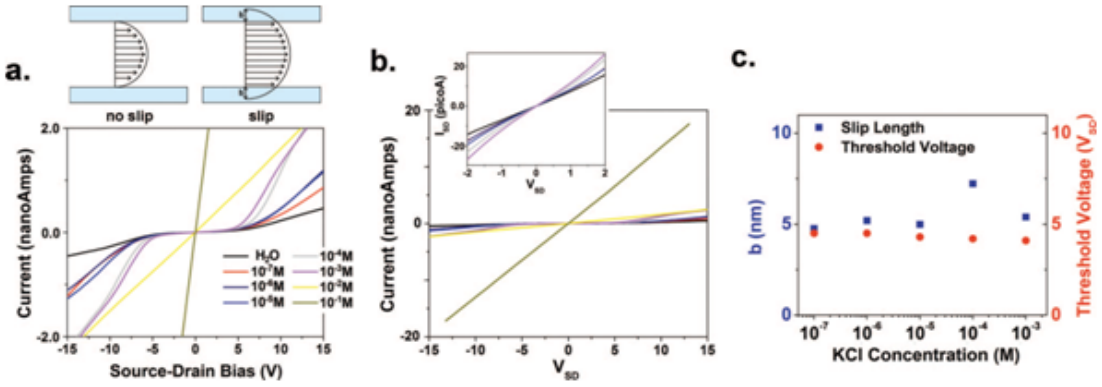

Figure 2.3. Source-drain current-voltage (I-V) data of the nanofluidic devices at various values of [KCl]. **a**. I-V curves for [KCl] from 10^{-7} to 10^{-1} M. The sharp increase in conductance at V_{SD} ~5 V for all curves for which [KCl] $\leq 10^{-3}$ M is interpreted as the onset of nonzero slip. Schematic diagrams show ion velocity profiles in both the low bias no-slip region and the high bias slip region. **b.** Source-drain I-V data plotted with an expanded current axis, illustrating conductance saturation for [KCl] $\leq 10^{-3}$ M. The saturation implies that, for those concentrations, the Debye screening length in the channel is larger than the channel width. Inset: Expanded I-V curves for [KCl] $\leq 10^{-3}$ M. Note the y-axis scale is picoamperes. The color coding of the traces is the same as in part a. **c.** Slip length (**b**) vs KCl concentration for [KCl] $\leq 10^{-3}$ M along with a display of the threshold voltage (V_T) above which slip occurs with respect to these same KCl concentrations.

In the surface charge-governed ion transport regime, [KCl]$\leq 10^{-3}$ M, and for V_{SD} values above a threshold voltage (V_T) of about 5 V, the current exhibits a sharp and nonlinear increase with increasing bias (**Figure 2.3a**) and conductance enhancement of 20-50 fold, depending upon [KCl]. We propose that this nonlinear behavior arises from an electric field-induced breakdown of the zero-slip condition. The transition into the finite-slip regime can be attributed to the changing behavior of the K^+ ion double layer in the nanochannel solution. The layer closest to the surface, called the Stern layer, is about 0.3 nm thick[26] and consists of K^+ ions immobilized to the nanochannel surface. The second layer, which can move under no-slip conditions, is a diffuse layer of K^+ ions that comprises the rest of the solution within the nanochannels[27] (**Figure 2.4a**).

However, it has been theorized that the Stern layer can be moved tangential to the surface under the influence of an external electric field[2,26] (**Figure 2.4b**). In our device, this may be happening above the threshold V_{SD}, in which case the electric field parallel to the nanochannel surface is overcoming the attraction of the Stern layer K^+ ions to the silica surface. As a result, these ions move along the surface, electroosmotically pulling water with them, and the zero-slip condition no longer holds. Due to viscous forces, hydrodynamic slip at the nanochannel surface increases the velocity of all species within the nanochannel, resulting in greatly enhanced conductance as illustrated in **Figure 2.4b** as well as in the schematic diagrams in **Figure 2.3a**.

Nonlinear I-V characteristics in somewhat larger (40 nm deep) nanofluidic channels for sodium phosphate concentrations in the range 10^{-4} – 10^{-2} M have been observed by Kim, et al[9]. However, their results reflect very different physics. They observed a broad, current-saturated, intermediate bias region separating their low- and high-bias regions. They interpret their data within the framework of concentration polarization, in which an ion depletion region develops at the microchannel/nanochannel interface, which leads to the current saturation regime in their I_{SD}-V_{SD} plots. At sufficiently high bias, instabilities (imaged as vortices) appear at the microchannel/nanochannel interface, collapsing the depletion regions, and resulting in a second phase of steep current increase (the overlimiting region). At even higher bias, conductance values return to their original (low-bias) levels. The lack of a current-saturated region in our data, the fact that conductances remain high and stable as V_{SD} increases, the absence of nonlinear ion transport above 10^{-3} M, and the below-described

voltage-gating experiments all distinguish our system and support the interpretation of non-zero slip in our channels.

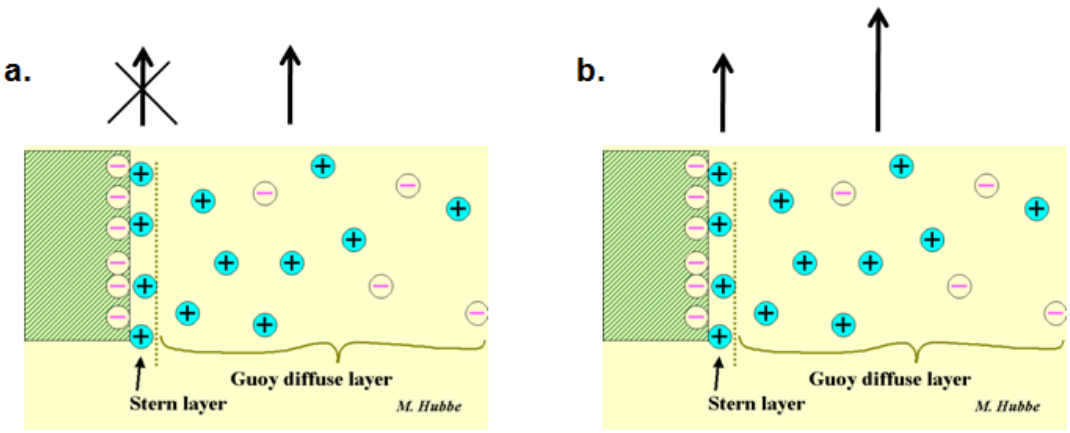

Figure 2.4. The effect of a high electric field on Stern layer ions. a. Stern layer counterions at the channel surface are normally immobolized by surface charges and do not contribute to the current. **b.** If Stern layer counterions can travel in the presence of a high electric field, the resulting finite slip at the channel surface allows enhanced velocity of diffuse layer ions via electro-osmosis and viscous forces. *Adapted from M. Hubbe, Dept. of Forest Biomaterials, NCSU.*

2.3.2 Nanochannel ion transport model

The contribution of slip to conductance enhancement within a nanochannel of radius comparable to the Debye screening length can be modeled as follows (see Appendix for detailed description). To maintain electroneutrality, the nanochannel surface charge must equal the counterion charge in the solution ($\mathbf{Q}_{surface} = \mathbf{Q}_{solution}$). This is expressed as:

$$\mathbf{A} \times \boldsymbol{\sigma} = \mathbf{V} \times \mathbf{e} \times \mathbf{n}_{cr} \qquad (1),$$

where **A** is the nanochannel surface area, $\boldsymbol{\sigma}$ is the surface charge density, **V** is the nanochannel volume, and $\mathbf{n}_{cr}$ is the critical ion density at which nanochannel ion transport transitions from bulk-like to a surface-charge governed regime (herein, $\mathbf{n}_{cr}$ is

equivalent to a K^+ concentration of ~10^{-3} M). The value of $\boldsymbol{\sigma}$ obtained is 0.0006 C/m^2. Using this value, the slip length **b** can be calculated using the conductance equation:

$$\mathbf{G} = \mathbf{N} \times 4\,\boldsymbol{\mu}\,\boldsymbol{\sigma}\,(\mathbf{d}/\mathbf{L})\,(1 + \mathbf{b}/l_{stern}) \qquad (2),$$

where $\boldsymbol{\mu}$ is the K^+ mobility (= 7.6×10^{-8} $m^2/(V\cdot s)$), **d** is the nanochannel hydraulic diameter (= 24 nm), **L** is the nanochannel length (=20 micrometers), **N** is the number of nanochannels (80) in the array, and l_{stern} is the thickness of the Stern layer (~0.3 nm), which is also the distance over which the shear plane moves when shifting from no-slip to slip conditions. The first part of equation (2), $\mathbf{N} \times 4\,\boldsymbol{\mu}\,\boldsymbol{\sigma}\,(\mathbf{d}/\mathbf{L})$, represents electrokinetic conductance through the nanochannels in the absence of slip, and the $(1 + \mathbf{b}/\,l_{stern})$ factor represents the conductance enhancement due to slip[1,2]. For conductance in the low bias ($V_{SD} < V_T$) regime, where there is no slip (**b** = 0), the measured conductance (~14.4 pS) is almost identical to the value calculated (~16.8 pS) using equations (1) and (2).

2.3.3 Tuning the nanochannel surface charge density by application of gate voltages

If the emergence of hydrodynamic slip is indeed a consequence of a field-induced breakdown in electrostatic attractions between the Stern layer and the channel wall, reducing the surface charge density should lower this electrostatic barrier and enhance slip. This reasoning is supported by two observations. First, there is no significant difference either in slip length or in the threshold voltage at which slip occurs for all values of [KCl]≤ 10^{-3} M (**Figure 2.3c**). This is attributable to the fact that the surface charge density remains fairly stable throughout these concentrations. Additional support stems from experiments that exploit a gate electrode to tune the nanochannel surface

charge density and measure the corresponding change in slip length. The gating experiments on a 10^{-4} M KCl solution are presented in **Figure 2.5**.

Another noteworthy observation is the reversal in the effect of V_g on conductance between the low bias and high bias regimes. As V_g becomes more positive, the bare surface charge density (σ) extracted from equation (1) becomes less negative (**Figure 2.5b**), which has two potentially competing effects. The first is a decrease in the intrachannel counterion concentration, which tends to *decrease* the conductance. The second is a decrease in the attraction of the Stern layer to the channel surface, which tends to *increase* the conductance (due to slip). At low source-drain bias ($V_{SD} < V_T$), the electric field is not strong enough to overcome the attraction of the Stern layer to the surface, so the decrease in ion concentration with increased V_g (**Figure 2.5a inset**) translates directly to a decreased conductance, as shown in previous studies[11,12]. By contrast, in the high source-drain bias ($V_{SD} > V_T$) regime, the electric field is strong enough to move the Stern layer. Therefore, as V_g becomes more positive, the Stern layer moves faster (larger slip length, **b**) (**Figure 2.5c**), resulting in a net increase in conductance. Alternatively, less force is required to begin moving the Stern layer (lower V_T) as its attraction to the channel surface decreases with more positive V_g.

Over the entire range of V_{SD}, the nonlinear nature of the I-V curves is evident for all values of V_g (**Figure 2.5a**). In the low bias regime ($V_{SD} < V_T$), where there is no slip, the ohmic response is well-described by the conductance equation without the enhancement factor (notice that the enhancement factor reduces to unity for **b** = 0) as shown in the Appendix. In the high V_{SD} regime ($V_{SD} > V_T$), these curves were fitted with the full conductance equation including the slip enhancement term illustrated in equation

(2). Such linear fits permitted us to extract the slip length, **b**, for each value of V_g (**Figure 2.5c**). Our obtained slip lengths in the range of ~2 – 10 nm are comparable to those proposed in studies of SiO_2 surfaces[28] and represent on average 8 – 35-fold increases in conductance.

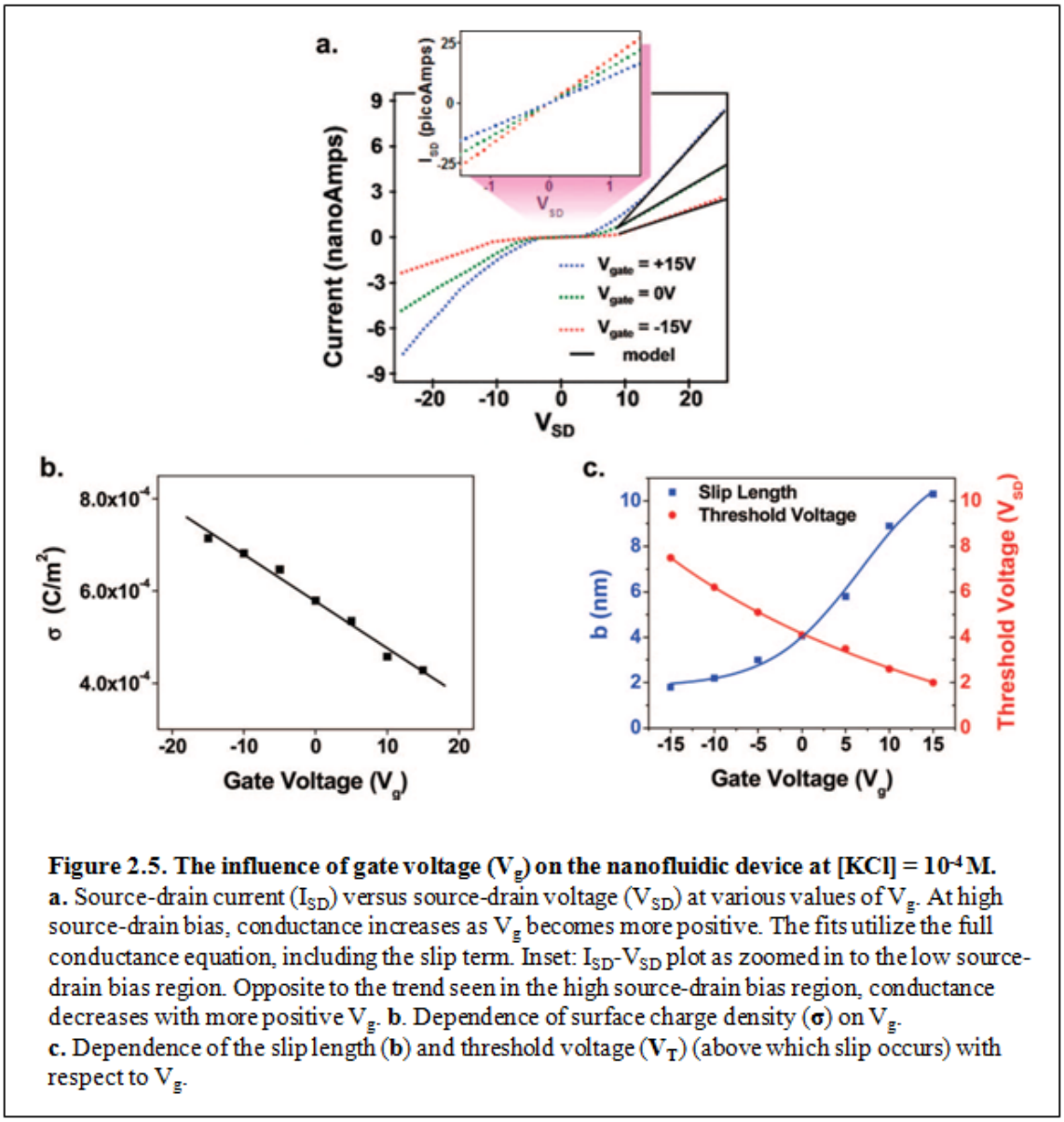

Figure 2.5. The influence of gate voltage (V_g) on the nanofluidic device at [KCl] = 10^{-4} M. **a.** Source-drain current (I_{SD}) versus source-drain voltage (V_{SD}) at various values of V_g. At high source-drain bias, conductance increases as V_g becomes more positive. The fits utilize the full conductance equation, including the slip term. Inset: I_{SD}-V_{SD} plot as zoomed in to the low source-drain bias region. Opposite to the trend seen in the high source-drain bias region, conductance decreases with more positive V_g. **b.** Dependence of surface charge density (**σ**) on V_g. **c.** Dependence of the slip length (**b**) and threshold voltage ($\mathbf{V_T}$) (above which slip occurs) with respect to V_g.

2.3.4 Peptide sequencing

A 10^{-4} M solution of aspartic acid monomers at a pH of 5.5 was inserted into the nanochannel array, and I-V curves were obtained. The device fabrication and measurement setup were identical to those used in I-V measurements with KCl. The data for the amino acid species under varying gate voltages (**Figure 2.6a**) is similar to that seen with 10^{-4} M KCl, with enhanced ion transport occurring above a threshold voltage, but, for aspartic acid, this increase is only observed under the influence of a positive gate voltage. For $V_g = 0$, the conductance is just starting to increase at V_{SD} above $|\pm 20$ V$|$, and for $V_g < 0$, this phenomenon is completely suppressed at all values of V_{SD}. At low source-drain bias, decreasing conductance with increasing V_g parallels the behavior of KCl **(Figure. 2.6a inset**) and emphasizes the opposite trend in conductance vs. gate voltage at low and high source-drain bias. The slip lengths range from 0 – 8 nm (**Figure 2.6b**), values that are comparable to those seen with KCl, although the suppression of the slip length at negative gate voltages is not seen with KCl under the V_{SD} range measured.

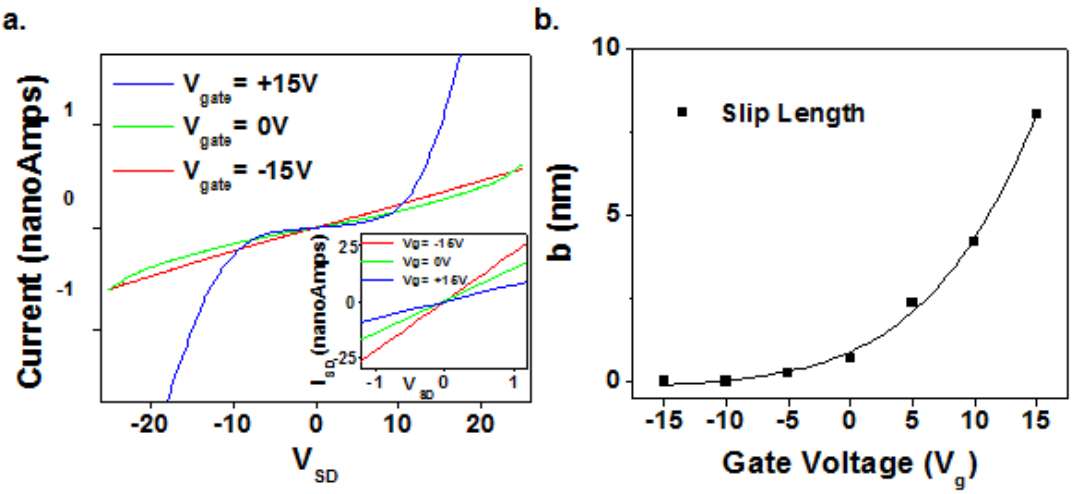

Figure 2.6. The influence of gate voltage (V_g) on the nanofluidic device at [Aspartic Acid] = 10^{-4} M. a. Source-drain current (I_{SD}) versus source-drain voltage (V_{SD}) at V_g = -15 V, 0 V, +15 V, with a V_{SD} sweep from -25 V to +25 V. Inset: Expanded I_{SD}-V_{SD} curves illustrating the dependence of conductance on V_g at low source-drain bias. **b.** Dependence of the slip length (**b**) on V_g. The slip length (**b**) increases as V_g is varied from -15 V to +15 V in 5 V increments.

However, the similarities between the measurements of the aspartic acid and KCl solutions indicate that positive ions are the dominant charge carriers in the aspartic acid solution. Above a pH of ~3.9, the majority of aspartic acid monomers are deprotonated, giving negatively charged aspartate ions and positive hydronium ions. The negative surface charge of the nanochannels with the ensuing Debye length on the order of the nanochannel radius prevents the entry of aspartate ions, in which case conductance is dominated by hydronium ions.

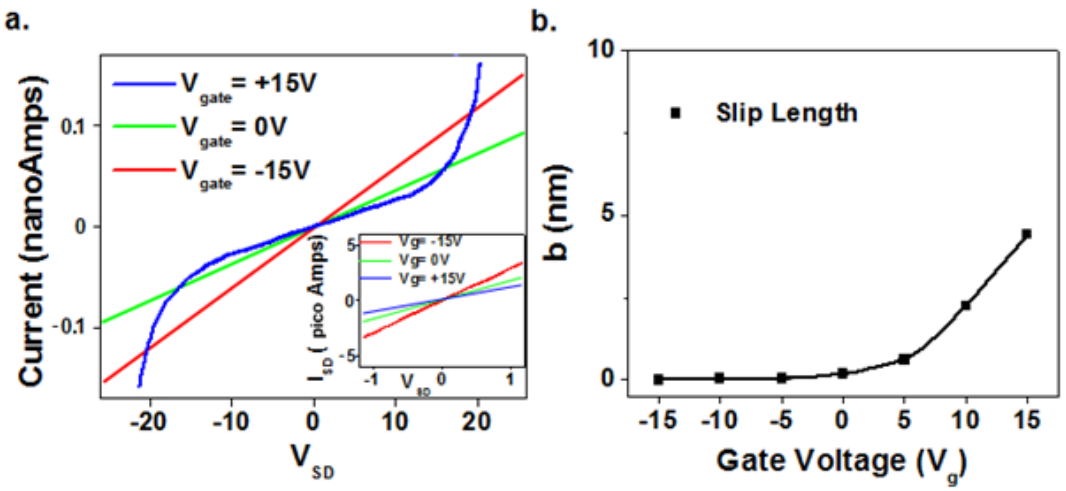

Figure 2.7. The influence of gate voltage (V_g) on the nanofluidic device at [Lysine] = 10^{-4} M. **a.** Source-drain current (I_{SD}) versus source-drain voltage (V_{SD}) at V_g = -15 V, 0 V, +15 V, with a V_{SD} sweep from -25 V to +25 V. Inset: Expanded I_{SD}-V_{SD} curves illustrating the dependence of conductance on V_g at low source-drain bias. **b.** Dependence of the slip length (**b**) on V_g. The slip length (**b**) increases as V_g is varied from -15 V to +15 V in 5 V increments.

A similar experiment was also conducted on a 10^{-4} M solution of lysine monomers at a pH of 9.0 (**Figure 2.7)**. Here, enhanced ion transport above a threshold voltage was observed as well, however the threshold voltage was considerably higher than for aspartate and was only significantly observed for $V_g > +5$ V (**Figure 2.7a**). Even at these positive gate voltages, the conductance just starts to increase at V_{SD} above |±30 V|, resulting in slip lengths that range from 0 – 5 nm (**Figure 2.7b**). Also, the values of the current are about an order of magnitude smaller than those seen for aspartate, signifying that the conducting species must be considerably larger in this case. Given these observations and the fact that below a pH of ~ 10.5, the majority of lysine monomers are protonated, positively charged lysine monomers are most likely the major conducting species. With the differences in I-V characteristics and slip lengths seen for aspartate and lysine, nanofluidic channels have great potential for identifying all the other amino acids

based on mass and pKa value. Once this is achieved, the obvious next step would be to sequence peptides.

2.3.5 Mechanical power enhancement

The ability to access finite-slip conditions in these nanochannels is encouraging from the point-of-view of energy conversion. We consider the mechanical power output of our device. This is the kinetic energy per unit time that is associated with the electroosmotic movement of fluid through the nanochannel array:

$$\textbf{Mechanical Power} = (\mathbf{1/2})(\rho \upsilon_{eof} A)\, \upsilon_{eof}^{\,2} \qquad (3),$$

where υ_{eof} is the electroosmotic fluid velocity of water through the nanochannels, and $\rho \upsilon_{eof} A$ is the mass flow rate. According to equation (3), the mechanical power increases as the cube of the electroosmotic fluid velocity. Therefore, an 80 – 200-fold increase in fluid velocity, as calculated in our device due to slip, translates to a ~10^6 enhancement in mechanical power. Detailed calculations on electroosmotic fluid velocity enhancements extracted from current measured in the nanochannel array device and their correlation to mechanical power are described in the Appendix. Such a large improvement in mechanical power through these silica channels suggests that they may also be useful for certain applications outside of peptide sequencing for which nanofluidic devices have been targeted, such as filtration and water desalination.

Based on our results showing enhanced ion transport, silica-based nanofluidic devices would likely exhibit a higher mechanical-to-electrical energy conversion efficiency than the current measured limit of 3 %[23]. In a recent work by Ren and Stein[21], theoretical characterization of electrokinetic transport through nanochannels showed that

streaming current increases dramatically with increases in slip length, predicting > 70 % energy conversion efficiencies. The ability to tune slip lengths with gate voltages should permit the testing of this theory in future experiments. Measurements of streaming currents through nanochannels will require a slight modification of our device design, since the PDMS/silica interface cannot tolerate high pressures.

2.4 Conclusion

In summary, we have investigated ion and amino acid transport through an array of 80 closely-spaced sub-20 nm hydrophilic SiO_2 nanochannels over a 30 – 50 V range of source-drain biases. We have observed that for ion concentrations at which the Debye length exceeds the nanochannel radius, ion transport becomes greatly magnified at a threshold source-drain bias. This behavior can be described by a theoretical model that attributes the enhancement to a breakdown of the no-slip boundary condition at the liquid/nanochannel surface interface at high source-drain bias. By varying the surface charge density of the nanochannels using a gate electrode, we were able to tune the slip length to obtain further enhancements in ion transport through the hydrophilic nanochannel array. Using this technique, we were also able to obtain specific I-V characteristics for two different amino acids, aspartate and lysine. These results imply that such devices have the potential to be utilized for protein sequencing and structure determination and can be harnessed for efficient energy conversion applications.

2.5 References

1. Bocquet, L.; Barrat, J. L. Flow boundary conditions from nano- to micro-scales. *Soft Matter*, **2007**, 3, 685-693.

2. Joly, L.; Ybert, C.; Trizac, E.; Bocquet, L. Liquid friction on charged surfaces: from hydrodynamic slippage to electrokinetics. *J. Chem. Phys.*, **2006**, 125, 204716.

3. Joseph, S.; Aluru, N. R. Why are carbon nanotubes fast transporters of water? *Nano Lett.*, **2008**, 8, 452-458.

4. Netz, R. R. Electrofriction and dynamic Stern layers at planar charged surfaces. *Phys. Rev. Lett.*, **2003**, 91, 138101.

5. Holt, J. K.; et al. Fast mass transport through sub-2-nanometer carbon nanotubes. *Science*, **2006**, 312, 1034-1037.

6. Lee, C.; Choi, C.; Kim, C. Structured surfaces for a giant liquid slip. *Phys. Rev. Lett.*, **2008**, 101, 064501.

7. Majumder, M.; Chopra, N.; Andrews, R.; Hinds, B. J. Nanoscale hydrodynamics: enhanced flow in carbon nanotubes. *Nature*, **2005**, 438, 44.

8. Cao, H.; et al. Fabrication of 10 nm enclosed nanofluidic channels. *Appl. Phys. Lett.*, **2002**, 81, 174-176.

9. Kim, S. J.; Wang, Y. C.; Lee, J. H.; Jang, H.; Han, J. Concentration polarization and nonlinear electrokinetic flow near a nanofluidic channel. *Phys. Rev. Lett.*, **2007**, 99, 044501.

10. Liang, X. G.; Morton, K. J.; Austin, R. H.; Chou, S. Y. Single sub-20 nm wide, centimeter-long nanofluidic channel fabricated by novel nanoimprint mold fabrication and direct imprinting. *Nano Lett.*, **2007**, 7, 3774-3780.

11. Fan, R.; Yue, M.; Karnik, R.; Majumdar, A.; Yang, P. D. Polarity switching and transient responses in single nanotube nanofluidic transistors. *Phys. Rev. Lett.*, **2005**, 95, 086607.

12. Karnik, R.; et al. Electrostatic control of ions and molecules in nanofluidic transistors. *Nano Lett.*, **2005**, 5, 943-948.

13. Stein, D.; Kruithof, M.; Dekker, C. Surface-charge-governed ion transport in nanofluidic channels. *Phys. Rev. Lett.*, **2004**, 93, 035901.

14. Powell, M. R.; et al. Nanoprecipitation-assisted ion current oscillations. *Nature Nanotech.*, **2008**, 3, 51-57.

15. Vlassiouk, I.; Siwy, Z. Nanofluidic diode. *Nano Lett.*, **2007**, 7, 552-556.

16. Kalman, E.; Vlassiouk, I.; Siwy, Z. Nanofluidic bipolar transistor. *Adv. Mater.*, **2008**, 20, 293-297.

17. Pennathur, S.; Santiago, J.G. Electrokinetic transport in nanochannels. 1. Theory. *Anal. Chem.*, **2005**, 77, 6772-6781.

18. Pennathur, S.; Santiago, J.G. Electrokinetic transport in nanochannels. 2. Experiments. *Anal. Chem.*, **2005**, 77, 6782-6789.

19. Baldessari, F.; Santiago, J.G. Electrophoresis in nanochannels: brief review and speculation. *J. Nanobiotechnology*, **2006**, 4, 12.

20. Pennathur, S.; Eijkel, J. C.; van den Berg, A. Energy conversion in microsystems: is there a role for micro/nanofluidics? *Lab Chip*, **2007**, 7, 1234-1237.

21. Ren, Y. Q.; Stein, D. Slip-enhanced electrokinetic energy conversion in nanofluidic channels. *Nanotechnology*, **2008**, 19, 195707.

22. Van der Heyden, F. H. J.; Bonthuis, D. J.; Stein, D.; Meyer, C.; Dekker, C. Electrokinetic energy conversion efficiency in nanofluidic channels. *Nano Lett.*, **2006**, 6, 2232-2237.

23. Van der Heyden, F. H. J.; Bonthuis, D. J.; Stein, D.; Meyer, C.; Dekker, C. Power generation by pressure-driven transport of ions in nanofluidic channels. *Nano Lett.*, **2007**, 7, 1022-1025.

24. Melosh, N. A.; et al. Ultrahigh-density nanowire lattices and circuits. *Science*, **2003**, 300, 112-115.

25. Chun, M. S.; Park, W. C. Time evolution of electrokinetic flow-induced streaming potential and flux in dead-end and cross-flow filtration of colloids through nanopores. *J. Membr. Sci.*, **2004**, 243, 417-424.

26. Gupta, A. K.; Coelho, D.; Adler, P. M. Influence of the Stern layer on electrokinetic phenomena in porous media. *J. Colloid Interface Sci.*, **2007**, 316, 140-159.

27. Fawcett, W. R. *Liquids, Solutions, and Interfaces: From Classical Macroscopic Descriptions to Modern Microscopic Details (Topics in Analytical Chemistry)* Oxford: Oxford Univ. Press, 2004.

28. Bonaccurso, E.; Kappl, M.; & Butt, H. J. Hydrodynamic force measurements: boundary slip of water on hydrophilic surfaces and electrokinetic effects. *Phys. Rev. Lett.*, **2002**, 88, 076103.

29. Delgado, A.V. *Interfacial Electrokinetics and Electrophoresis*. New York: Marcel Dekker, 2002.

30. Lyklema, J. *Fundamentals of Interface and Colloid Science, Vol. II*. London: Academic Press, 1995.

31. Israelachvili, J. N. *Intermolecular and Surface Forces*. London: Academic Press, 1992.

32. Vlassiouk, I.; Smirnov, S.; Siwy, Z. Ionic selectivity of single nanochannels. *Nano Lett.*, **2008**, 8, 1978-1985.

2.6 Appendix A: Nanochannel Fabrication and Measurement

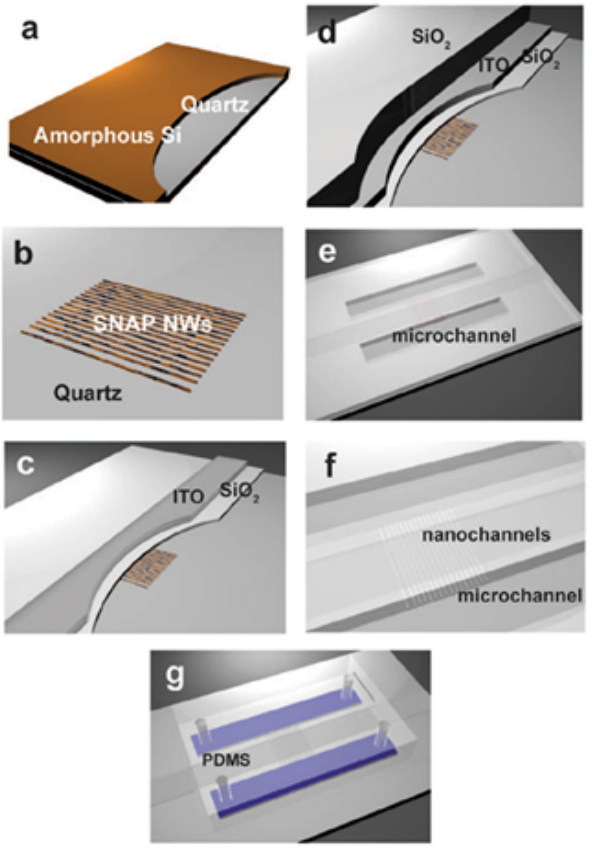

Figure 2.8
Nanochannel device fabrication. **a.** 1 x 1 inch quartz wafer with a 30 nm thick amorphous silicon layer. **b.** A 5 μm wide array of 80 SNAP nanowires patterned from the amorphous silicon layer. **c.** A 40 nm thick low temperature oxide gate oxide layer is deposited onto the nanowire array followed by deposition and patterning of an indium tin oxide gate electrode. **d.** A 5.5 μm thick low temperature oxide layer is deposited next. **e.** Microchannels are etched through the low temperature oxide all the way down to the level of the nanowires. **f.** Nanochannels are created by XeF_2 etching of the silicon nanowires. **g.** A PDMS slab with input and output holes is aligned over the microchannels and plasma bonded to the wafer. Ionic solutions and Ag/AgCl electrodes are inserted into microchannel inputs on both sides of the nanochannels.

The first step in building nanochannels (**Figure 2.8**) was to generate a nanowire template. The SNAP method[24] and standard electron beam lithography (EBL) were used to make an array of silicon nanowires on a transparent quartz substrate with a 30 nm-thick amorphous silicon layer deposited using an e-beam evaporator. In the silicon nanowire array generated by the SNAP method, each wire was about 15 – 20 nm-wide with a pitch of 50 nm. The wires were sectioned into regions 20 μm in length and 5 μm in

width by standard electron beam lithography (EBL). Low Pressure Chemical Vapor Deposition (LPCVD) was then used to deposit a 40 nm-thick silicon dioxide gate oxide layer on top of and between the wires according to the reaction: $SiH_4 + O_2 \rightarrow SiO_2 + 2H_2$. A 50 nm-thick layer of indium tin oxide (ITO) was sputtered on top of the low temperature oxide (LTO), patterned with photoresist, and etched with a 0.5 M HCl solution to create the gate electrode. A 5 μm-thick layer of LTO was deposited on top of the device. Photoresist was spun onto the LTO layer and a microchannel pattern was made by photolithography. The pattern was etched down via an Active Oxide Etching (AOE) process (CHF_3:C_4F_8:Ar = 33 sccm:7 sccm:10 sccm, 200 W, 10 mTorr, 15 minutes) to expose the ends of the SNAP wires. This gave a set of microchannels connecting either end of the SNAP wires. The microchannel depth was about 5.5 μm as confirmed by a surface profiler (Dektak 150). The photoresist was stripped by acetone, and the substrate was further cleaned by a piranha solution (H_2SO_4: H_2O_2 = 5:1 by volume). At this point, XeF_2 was used to selectively and isotropically etch the silicon wires to form hollow channels within the glass according to the reaction: $2XeF_2 + Si \rightarrow SiF_4(g) + 2Xe(g)$. Before loading substrates into the XeF_2 etching chamber, the substrates were dipped into a buffered oxide etching solution (BOE: NH_4F/HF= 6:1 by volume) for 1 second to remove native oxide layers on the exposed tips of the silicon wires. The pressure of XeF_2 gas was maintained at about 2800 mTorr during the etching procedures. The etching progress was monitored by a color change in the array as viewed by optical microscopy. Finally, PDMS with drilled input/output holes was bonded to the device by using an oxygen plasma technique to create a watertight seal between the microchannels. This seal ensures that the only connection between the microchannels is via the

nanochannels. Ionic solutions were inserted through the input holes in the PDMS, and the ionic current measurements were carried out with the use of a source/preamplifier unit (Keithley 2400). Commercially available Ag/AgCl electrode assemblies (E. W. Wright) were used. The ensuing electrokinetic current could be read, thereby allowing the characterization of ionic transport through the nanochannels.

2.7 Appendix B: Conductance Equation Derivation

The contribution of slip to conductance enhancement within a nanochannel of radius comparable to the Debye screening length can be modeled as follows. To maintain electroneutrality, the nanochannel surface charge must equal the counterion charge in the solution. This is expressed as:

$$\mathbf{Q}_{surface} = \mathbf{Q}_{solution} \qquad \text{(eq. A1).}$$

This fundamental equation can be expanded to show its components, which gives:

$$\mathbf{A} \times \sigma = \mathbf{V} \times \mathbf{e} \times (\mathbf{n_K} + \mathbf{n_{Cl}}) \qquad \text{(eq. A2),}$$

where **A** is the nanochannel surface area, σ is the surface charge density, **V** is the nanochannel volume, **e** is the electron charge, and $\mathbf{n_K}$ and $\mathbf{n_{Cl}}$ are the K^+ and Cl^- ion densities, respectively. For [KCl] ≤ 10^{-3} M, the interior of the nanochannel is virtually unipolar, made up almost entirely of K^+ ions, so that the term $\mathbf{n_{Cl}}$ becomes negligible. The factor $\mathbf{n_K} + \mathbf{n_{Cl}}$ can then be approximated as the parameter $\mathbf{n_{cr}}$, which is defined as the critical ion density within the nanochannel at which ion transport transitions from bulk-like to a surface charge-governed regime (herein, $\mathbf{n_{cr}}$ is equivalent to a K^+ concentration of ~10^{-3} M). Using these conditions along with eq. A2, the surface charge density (σ) of a single nanochannel for $[KCl]_{bulk} \leq 10^{-3}$ M is estimated as a function of $\mathbf{n_{cr}}$ by

$$\sigma = \frac{\mathbf{V} \times \mathbf{e} \times \mathbf{n_{cr}}}{\mathbf{A}} \qquad \text{(eq. A3),}$$

which gives a value of 0.0006 C/m^2. From the ion density, it is possible to find the current (**I**) associated with ion transport through a nanochannel, which is approximated as[29]

$$\mathbf{I} = \mathbf{e} \times \mathbf{n} \times \mu \times \mathbf{E} \times \mathbf{S} \qquad \text{(eq. A4)},$$

where **n** is the ion density, **μ** is the K^+ mobility (= 7.6×10^{-8} m^2/(V·s)), **E** is the electric field defined by source-drain voltage/nanochannel length ($\mathbf{V_{SD}/L}$), and **S** is the cross-sectional area of the nanochannel. The conductance (**G**) of the nanochannel array in the surface charge-governed regime at low source-drain bias is obtained by taking the derivative of the current with respect to source-drain voltage ($\mathbf{V_{SD}}$), treating the ion density (**n**) as $\mathbf{n_{cr}}$, and using eq. A3 to make the conductance a function of the surface charge density, which gives

$$\mathbf{G} = \mathbf{N} \times 4\,\mu\,\sigma\,(\mathbf{d/L}) \qquad \text{(eq. A5)},$$

where **d** is the nanochannel hydraulic diameter (= 24 nm), **L** is the nanochannel length (= 20 micrometers), and **N** is the number of nanochannels (80) in the array. To account for enhanced ion transport at high source-drain bias, eq. A5 is modified to

$$\mathbf{G} = \mathbf{N} \times 4\,\mu\,\sigma\,(\mathbf{d/L})\,(\mathbf{1} + \mathbf{b}/l_{stern}) \qquad \text{(eq. A6)},$$

where **b** is the extrapolated slip length, and l_{stern} is the thickness of the Stern layer (~0.3 nm), which is also the distance over which the shear plane moves when shifting from no-slip to slip conditions. The relation shown in eq. A5, $\mathbf{G = N \times 4\mu\sigma(d/L)}$, represents electrokinetic conductance through the nanochannels without considering slip (**b** = 0), as shown in **Figure 2.9**. The extra term, $1 + \mathbf{b}/l_{stern}$, presented in eq. A6, represents the

conductance enhancement due to slip[1,2]. For conductance in the zero-slip regime, the measured conductance (~14.4 pS) was almost identical to the value (~16.8 pS) obtained using eqs. A3 and A5.

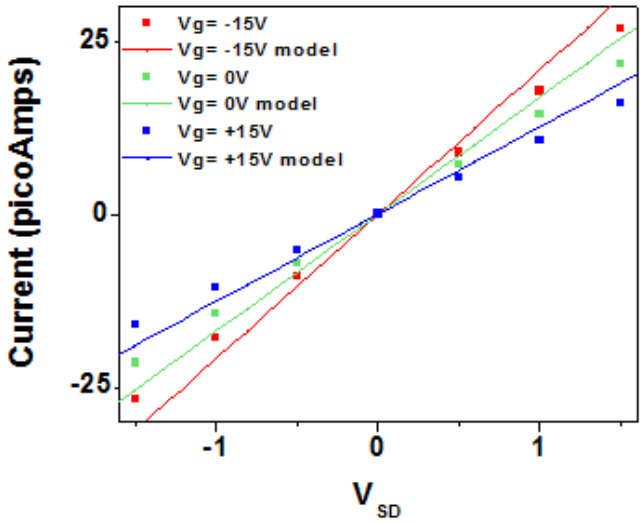

Figure 2.9. Model of gated KCl I_{SD}-V_{SD} curves. I-V curves were obtained for the nanochannel array at low source-drain bias for V_g = -15 V, 0 V, and +15 V. Squares represent experimental data points, and solid lines are based on a calculation of the conductance equation (eq. A5) without the slip-enhancement term so that **b** = 0.

2.8 Appendix C: Mechanical Power Calculations

The mechanical power output of the device – the kinetic energy per unit time associated with electroosmotic movement of fluid through the nanochannel – is defined by

$$\textbf{Mechanical Power} = \frac{1}{2}(\rho \upsilon_{eof} A)\upsilon_{eof}^2 \qquad \text{(eq. A7)},$$

where υ_{eof} is the electroosmotic flow velocity, ρ is the fluid density, A is the cross-sectional area, and $\rho\upsilon_{eof}A$ is the mass flow rate. To obtain the mechanical power output enhancement from the nanochannel device at high electric fields, we first calculate the electroosmotic flow velocity (υ_{eof}) of a KCl solution with a saturated nanochannel concentration of 10^{-3} M in the low voltage no-slip region and in the absence of a gate voltage by applying the Helmholtz-Smoluchowski equation[30]:

$$\upsilon_{eof} = \frac{\zeta \varepsilon E}{\eta} \qquad \text{(eq. A8)},$$

with η the viscosity of water, ε the permittivity, and E the electric field. ζ is the zeta potential at the shear plane, which can be derived from our previously calculated surface charge density (σ) via the Grahame equation[31]:

$$\sigma^2 = \frac{\varepsilon k_B T}{\pi} n_0 \left[\cosh \frac{e \zeta}{k_B T} - 1\right] \qquad \text{(eq. A9)},$$

where $k_B T$ is the thermal energy, and n_0 is the ion charge density within the nanochannels. This gives an electroosmotic velocity of 3.25×10^{-4} m/s at a source-drain bias of 1 volt.

The electroosmotic current (I_{eof}) can be determined from the electroosmotic velocity value by

$$I_{eof} = n_0 \upsilon_{eof} S \qquad \text{(eq. A10)},$$

where S is the cross-sectional area of all 80 nanochannels, resulting in a value of 1.5 picoAmps. This makes up roughly 10 % of the total experimentally measured current of 14.4 picoAmps at 1 volt, although electroosmotic flow has been theoretically shown to contribute up to 25 % of ion current in nanochannels[32].

Thus, assuming that electroosmotic flow accounts for between 10 % and 25 % of the total current, a linear extrapolation of the current from the no-slip, low bias region to higher voltage values results in an electroosmotic velocity of approximately 0.008 – 0.02 m/s at 25 volts. Extracting out the slip-enhanced velocity from the current in the experimental KCl I-V curve with V_g = +15 V shown in **Figure 2.5** using eq. A10 gives a value of ~1.7 m/s at 25 volts. We assume that electroosmotic flow dominates the current above the slip threshold voltage, so that the velocity value of 1.7 m/s is the electroosmotic velocity. Therefore, fluid velocity is enhanced about 80 – 200 times.

We can convert the velocity increases into mechanical power enhancement using eq. A7 above, which shows that mechanical power increases as the cube of the electroosmotic fluid velocity. Comparing slip-enhanced fluid flow to fluid transport confined by the no-slip boundary condition results in a calculated mechanical power output enhancement factor of approximately $5 - 6$ orders of magnitude at 25 volts.

2.9 Appendix D: Differential Conductance of Potassium Chloride

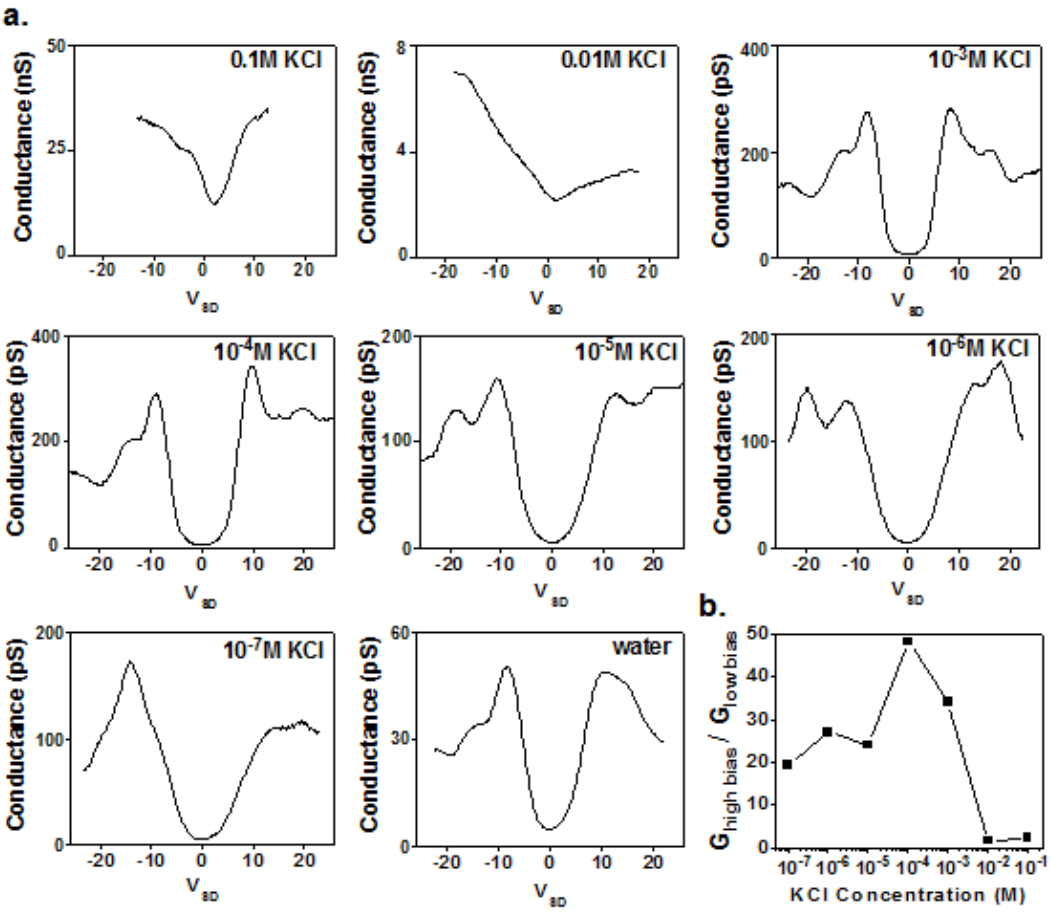

Figure 2.10. KCl differential conductance plots. **a.** Differential conductance curves for [KCl] from 10^{-1} M to 10^{-7}M and for water with a V_{SD} sweep from -25 V to +25 V. For [KCl] ≤ 10^{-3}M, the conductance plots exhibit a distinctive well shape, reflecting the nonlinear nature of the KCl I-V curves. A first (positive bias) conductance maximum occurs at V_{SD} ~ 8.5 V for [KCl] = 10^{-3}M. As [KCl] is reduced to 10^{-7}M, the well shape broadens, and that conductance maximum shifts gradually to higher voltage. **b.** A plot of the conductance increase versus [KCl]. For this plot, the value of the conductance, averaged over a 1 V range centered at the first conductance maximum, is divided by the conductance at low bias, averaged between -1 V and +1 V. The conductance increases between 20-fold and 50-fold, depending upon [KCl].